PAPER • OPEN ACCESS

Development and characterization of modular mouse phantoms for end-to-end testing and training in radiobiology experiments

To cite this article: Marie Wegner *et al* 2023 *Phys. Med. Biol.* **68** 085009

IOP Publishing Phys. Med. Biol. 68 (2023) 085009 https://doi.org/10.1088/1361-6560/acc566

Physics in Medicine & Biology

IPEM Institute of Physics and Engineering in Medicine

OPEN ACCESS

RECEIVED
13 December 2022

REVISED
1 March 2023

ACCEPTED FOR PUBLICATION
17 March 2023

PUBLISHED
5 April 2023

PAPER

Development and characterization of modular mouse phantoms for end-to-end testing and training in radiobiology experiments

Marie Wegner[1,2,*], **Thorsten Frenzel**[2,3], **Dieter Krause**[1] and **Elisabetta Gargioni**[2]

[1] Institute of Product Development and Mechanical Engineering Design, Hamburg University of Technology, Hamburg, Germany
[2] Department of Radiotherapy and Radiation Oncology, University Medical Center Hamburg-Eppendorf, Hamburg, Germany
[3] Mildred-Scheel-Cancer Career Center Hamburg, University Cancer Center Hamburg—Hubertus Wald Tumorzentrum, University Medical Center Hamburg-Eppendorf, Hamburg, Germany
[*] Author to whom any correspondence should be addressed.

E-mail: marie.wegner@tuhh.de

Keywords: mouse phantom, small-animal irradiation, additive manufacturing, dosimetry, Monte Carlo simulation

Abstract

Objective. In radiation oncology, experiments are often carried out using mice as a model for *in vivo* research studies. Due to recent technological advances in the development of high-precision small-animal irradiation facilities, the importance of quality assurance for both dosimetry and imaging is increasing. Additive manufacturing (AM) offers the possibility to produce complex models from a three-dimensional data set and to build cost-effective phantoms that can easily be adapted to different purposes. The aim of this work was therefore to develop detailed anatomical mouse models for quality assurance and end-to-end testing of small-animal irradiation and imaging by means of AM. *Approach*. Two mouse phantom concepts were designed, constructed, and examined for this purpose. The first model includes cavities corresponding to the most important organs. The final solid model was constructed using AM in two separate parts that can be attached with a plug connection after filling these cavities with tissue-equivalent mixtures. Moreover, different radiation dosimeters can be placed in the lower part of the model. For the second concept, AM was used for building modules like the phantom outer shell and bones, so that different mixtures can be used as a filling, without modifying the phantom structure. *Main results*. CT as well as Micro-CT scans of both concepts showed an excellent quality and adequate image contrast, with material attenuation properties close to those of mouse tissues, apart from the current bone surrogates. Radiation dose measurements with radiochromic films were, with some exceptions in areas with larges bone volumes, in agreement with calculations within less than ±4%. *Significance*. AM shows great potential for the development of mouse models that are inexpensive, easy to adapt, and accurate, thus enabling their use for quality assurance in small-animal radiotherapy and imaging. The introduction of such 3D-printable mouse phantoms in the workflow could also significantly reduce the use of living animals for optimization and testing of new imaging and irradiation protocols.

1. Introduction

Recent technological advances in the field of small-animal radiotherapy led to the development of sophisticated irradiation platforms for adapting pre-clinical research to the new radiotherapy standards and, among others, for better understanding the biological effects of partial volume irradiations with non-uniform dose. Such precise irradiation platforms should meet some important technical requirements, such as the availability of integrated imaging, targeted and/or modulated dose delivery, as well as accurate dose calculation (Verhaegen *et al* 2018). As a consequence, adequate quality assurance methods should be established in order to guarantee an optimal use and the correct mimicking of clinical radiotherapy treatments. In particular, a standard dose verification and report protocol for pre-clinical experiments is of major importance to ensure reliability and reproducibility of the data and the validity of intercomparison studies.

In the last years, several authors addressed this issue and the crucial importance of precise dosimetry of radiobiology experiments (Desroisers et al 2013, Pedersen *et al* 2016, Verhaegen *et al* 2018, Biglin *et al* 2019, Ghita *et al* 2019, Soultanidis *et al* 2019, Esplen *et al* 2019a, Esplen et al 2019b, Gronberg *et al* 2020, Silvestre Patallo *et al* 2020). Desrosier *et al* (2013) reported on discussions and recommendations that emerged during a workshop (sponsored in 2011 by the US National Institute of Allergy and Infectious Diseases, the National Cancer Institute and the National Institute for Standards and Technology) on the status and further necessary actions related to dose measurement and report in radiobiology. Even though the authors analyzed a small sample of publications in a specific journal, they showed, among other data, that the used dosimetry method during the experiments was reported only in 37% of cases, while the irradiation geometry and dose uncertainty were found in just 48% and 4% of papers, respectively. During the mentioned workshop, participants emphasized the importance of dosimetry comparison programs, appropriate training in radiation dosimetry for radiobiologists, as well as close collaboration between radiobiologists and medical physicists. Furthermore, the radiobiology community was strongly recommended to report on dosimetry, dose determination, radiation source properties, and irradiation geometry in research papers.

Since then, a few intercomparison studies were carried out to verify dose delivery with small-animal irradiators and to collect information about available resources and equipment (Pedersen *et al* 2016, Seed *et al* 2016, Gronberg *et al* 2020, Silvestre Patallo *et al* 2020). Pedersen *et al* (2016) designed cylindrical acrylical small-animal phantoms that can include calibrated thermoluminescence dosimeters (TLDs) and could be sent by mail to 12 irradiation facilities to verify their dose output. The results show that in seven institutions the measured dose deviated from the expected dose by more than $\pm 5\%$. A similar exercise was conducted by Seed *et al* using a two-phase process that consisted first in testing the use of optically-stimulated luminescence (OSL) dosimeters in mouse cadavers and, in a second phase, TLDs in cylindrical acrylic phantoms. In this case, four of the seven participants were able to deliver doses that differed less than $\pm 5\%$ from the expected values.

Recently, Gronberg *et al* (2020) developed robust polystirene phantoms that can either be used to calibrate a small-animal irradiator or be sent via mail for dosimetry audits. In the first case, the phantom has an insert for accommodating an ion chamber, which allows for absolute dose measurements according to international protocols. For dosimetry audits, the phantom can incorporate TLDs, that can be cross-calibrated using the ion chamber and then sent to other institutions. Additionally, Gronberg *et al* (2020) asked three intitutions, which used the same small animal irradiator and where a physicist could properly perform machine calibration and beam quality, to scan the phantom with their usual imaging protocols for treatment planning and to develop a treatment plan with specified dose, depth, and delivery techniques. This pilot study, altough small in dimensions and with some methodic limitations, revealed the feasibility of a mail audit and dose delivery within $\pm 7\%$ of the prescribed value.

These investigations point out that more work in terms of training and qualification of small-animal irradiator users is necessary to achieve a high reproducubility and validity of pre-clinical experiments, also by keeping in mind the ethical issue of the '3R' in animal research (Replacement, Reduction and Refinement) (Russel and Burch 1959). Moreover, as irradiation techniques and devices keep evolving, it became evident that physical phantoms play an essential role in this endeavour, not only for dosimetry purposes but also for evaluating image registration procedures and their influence on the overall uncertainty of delivered dose and tumour delineation (Verhaegen *et al* 2018). As a consequence, the physical properties of small-animal phantoms should be adapted for use both in dosimetry and multimodal imaging, also in view of the fact that some small-animal irradiation platforms are currently provided with integrated CT and bioluminescence (BL) imaging (Ghita *et al* 2019).

Due to small dimensions and the necessity of increasing the number of anatomical details, the construction of multi-purpose phantoms is still limited but is rapidly growing. One of the first detailed mouse phantoms for radiation dosimetry and x-ray imaging was designed by Welch *et al* (2015), who used computer-controlled micro-milling to produce a detailed anatomical model, which is modular and flexible and was produced using materials that can mimick x-ray absorption properties of soft tissue, lung, and bones, respectively, thus allowing for accurate dose measurements. However, micro-milling requires the availability of expensive machines and the proposed phantom is less flexible for use with other imaging modalities. In the meantime, growing attention is being turned to the development of realistic models by using additive manufacturing (AM), commonly known as 3D printing. These techniques support the use of computer-aided design (CAD) software to design three-dimensional models and manufacture objects of any complex shape (Ventola 2014, Filippou and Tsoumpas 2018, Tino *et al* 2019). In particular, for medical applications, it is possible to convert 3D diagnostic images into specific volume models that can be then managed by a 3D printer. This conversion usually involves several steps, such as image processing and mesh refinement, that, together with the selected printing technique, can affect the accuracy of the manufactured object (Filippou and Tsoumpas 2018).

Compared to other manufacturing methods, such as micro-milling, micro-machining, casting, and injection molding, AM is involved with less start-up costs and offers high flexibility with respect to both the anatomical details to be included (body shape and internal structure) and to the material choice for mimicking tissue properties (e.g. x-ray absorption, light scattering, or magnetic relaxation times). Finally, 3D printing can be used both directly (for printing phantoms) or indirectly (for printing phantom moulds), thus enabling an accurate an reproducible realisation of multi-purpose models (Ventola 2014, Filippou and Tsoumpas 2018, Tino *et al* 2019, Wegner *et al* 2021).

The recent small-animal phantom developments for radiation dosimetry were reviewed by Esplen *et al* (2019a, 2019b), who also produced a new model through exclusive use of 3D printing. The authors scanned a mouse bearing a flank subcutaneous tumour at the micro-CT unit of the Small Animal Radiation Research Platform (SARRP) (Xstrahl Ltd, Surrey, UK) and included several anatomical structures in the model, such as bones, soft tissue, and lungs. Their phantom, whose body and bones are printed using appropriate acrylic materials, is transversally cut into two parts through the middle of the lungs and can accommodate plastic scintillator dosimeters as well as a radiochromic film for dose verification. In addition, the authors performed detailed Monte Carlo simulations of seven irradiation treatments at the SARRP with different collimations and geometries, showing a good agreement between calculated and measured dose in different anatomical sites, such as brain, lungs, and abdomen. Despite the fact that the authors chose PMMA-like material to print the phantom parts corresponding to soft tissue and bones, they could show that discrepancies between dose measurements and calculations did not exceed $\pm 3.5\%$. Similar approaches were adopted by Soultanidis *et al* (2019) and Price *et al* (2020), who put much more attention into choosing tissue-mimicking materials, in particular for the 3D printing of bones, and in the detailed material characterization in terms of x-ray attenuation and CT numbers. It is important to mention that Price *et al* (2020) made their printable model available to the scientific community, thus offering a high degree of flexibility and reproducibility for future use with other treatment modalities and for advanced radiology. This phantom, for example, enabled Silvestre Patallo *et al* (2020) to investigate the accuracy of dose delivery at five UK institutions conducting radiobiology experiments with the SARRP. However, the current model does not allow for 2D dosimetry with films and, to our current knowledge, its use was demonstrated for target volumes in the mouse head only (Silvestre Patallo *et al* 2020).

In the field of multi-modality imaging, a thorough study was recently published by Zhang *et al* (2018). Starting from the micro-CT scan of a healthy mouse, these authors realised a phantom that consists of a 3D-printed skeleton and a skin shell. The skeleton is attached to the phantom skin shell and the inner volume filled with an hydrogel that was produced ad hoc as a soft tissue surrogate. The designed phantom is appropriate for CT, MR, and PET imaging but is not intended for use in radiation dosimetry. Advanced models are also available for optical imaging: Diep *et al* (2015) and Bentz *et al* (2016a, 2016b) printed heterogeneous 3D phantoms with different degrees of complexity, specifically for diffuse optical imaging and deep tissue fluorescence imaging. However, also in this case, the use in radiation dosimetry or for other imaging techniques is not considered.

To summarize the recent developments in this fields, made possible by the widespread use of additive manufacturing, each group has worked to design phantoms fulfilling specific requirements. The aim of this study was, instead, to design, produce, and characterize multi-purpose mouse phantoms, which are inexpensive, modular, and suitable for training, quality assurance, and refining of radiobiology experiments. In particular, we focus on a general design, which enables users to easily adapt the internal structure of the phantom. This is made possible by downloading the available volume models, as described below, and adding up or deleting desired components. The two prototypes proposed in this study are designed using AM, with special attention devoted to obtain flexible, cost-effective phantoms, both for dosimetry and imaging. These phantoms are suitable for each step of a typical workflow in small-animal irradiation and imaging, including 2D/3D dosimetry and can be manufactured by using a single volume model. Moreover, on a longer term, they can be easily adapted to multiple imaging modalities, just by changing the tissue surrogates, while maintaining the original phantom structure.

2. Materials and methods

2.1. Volume model and material choice

The criteria that we considered during the phantom design were (i) a high level of anatomical details, (ii) heterogeneous material composition, (iii) adequacy for treatment planning and dosimetry, (iv) adequacy for CT imaging, (v) low cost, and (vi) flexibility.

In a first step, a volume model of the mouse body and main inner structures, as can be seen in figure 1, was built on the basis of the 3D open-source digital mouse atlas *Digimouse* (Dogdas *et al* 2007). We used the open-source software packages *3D Slicer* (Brigham Women's Hospital, Boston, MA) for importing the mouse atlas, and *Autodesk Meshmixer* (Autodesk, San Rafael, CA) for smoothing and further preparation. The volume model

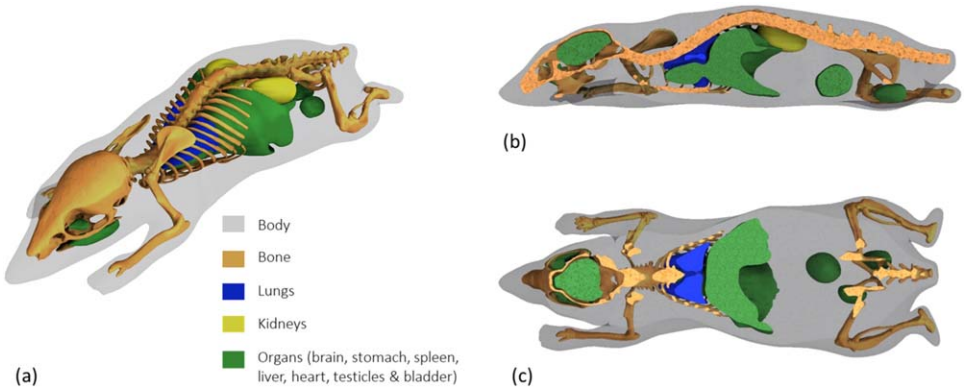

Figure 1. Phantom volume model, obtained from the digital mouse atlas 'Digimouse'. Three-dimensional perspective with defined sub-volumes corresponding to different tissues/organs(a), sagittal view (b), coronal view (c).

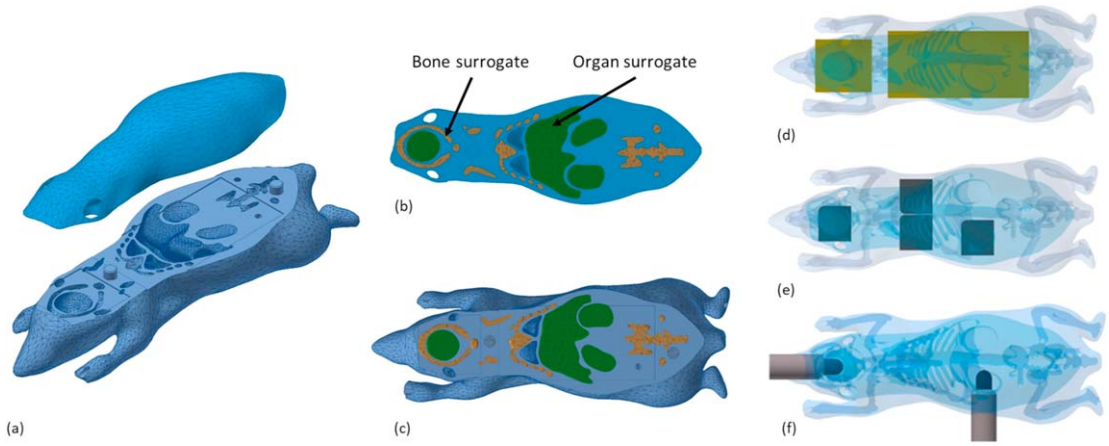

Figure 2. Phantom design process: CAD-concept for C1 (a). While the upper part is standard (b), the lower part can be adapted to accommodate different dosimeters at different positions(c)–(f). Moulds are modelled in correspondence of bones and relevant organs, that can be filled with tissue-equivalent materials (b)–(c).

consists of outer surface, skeleton, lungs, kidney, brain, urinary bladder, and testicles. Moreover, the heart and other inner organs in the gastrointestinal tract, such as stomach, spleen, and liver, were connected for simplicity to form a single volume, but they could be split for specific purposes.

2.2. Development of two different modular product families

We followed two strategies during the phantom development. A first phantom (referred to as *Concept* 1) was manufactured in such a way, that the full material composing the body contains cavities corresponding to relevant inner organs that can be filled with different tissue-equivalent materials. In this case, the phantom could be mainly used for radiation dosimetry purposes or for imaging modalities based on x-ray absorption and scattering, such as CT. A second one (*Concept* 2) consists of modules representing the skin (or body shell), a full-material skeleton, and an inner shell containing relevant organs. This phantom can otherwise be filled with tissue-equivalent surrogates. This will allow, in the future, both radiation dose measurements and multi-modal imaging, e.g. CT combined with MRI or BLI.

2.2.1. Design of concept 1 (C1)

For designing the first phantom, the volume model (as seen in figure 1) was split into two parts on the coronal plane using *Autodesk Inventor* (Autodesk, San Rafael, CA). While the upper part is a standard part, the lower one is variant and can be easily adapted to accommodate not only radiochromic films, but also other dosimeters that can be placed in different areas of the body (figure 2). The two parts are attached to each other using plug connectors as interfaces.

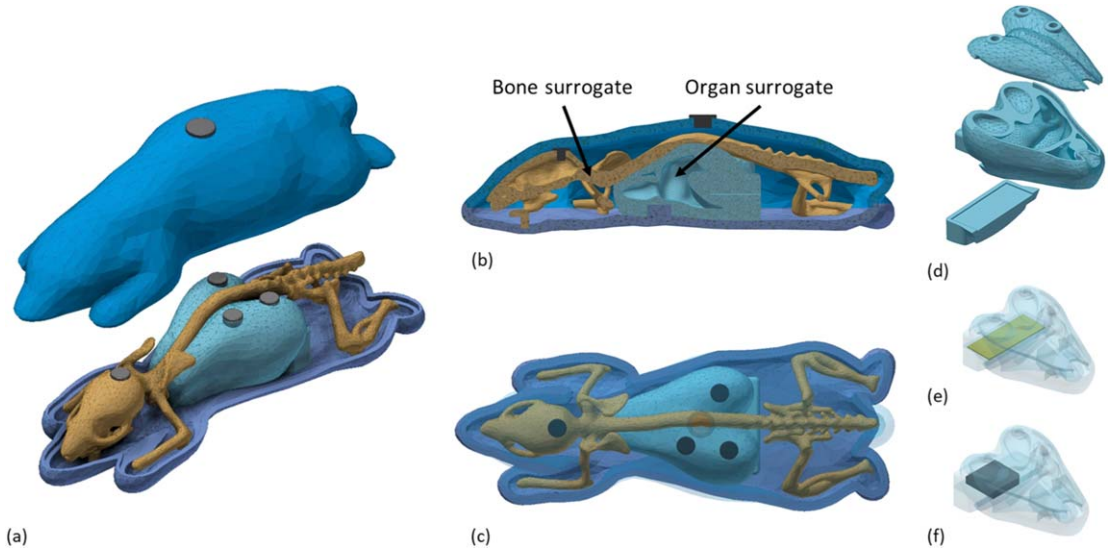

Figure 3. Phantom design process: CAD-concept for C2 (a). A body shell, the skeleton, and a shell containing relevant organs are separately modelled and can reproducibly be connected to each other (a)–(c). The shells (in blue) can be filled up with tissue-equivalent gels and closed with 3D-printed plugs (in black). The variant part of the organ shell (d) can be adapted for accommodating a dosimeter (e)–(f).

2.2.2. Design of concept 2 (C2)

For implementing the second phantom, we designed the body shell, the skeleton, and a shell for inner organs as objects to be 3D printed (also designed using *Autodesk Inventor*). The skeleton can be fixed to the lower part of the outer shell via plug connectors, while the inner shell containing further organs is split into two parts and can also be fixed to the outer shell and the skeleton via plugs (figure 3). Furthermore, the inner and outer shell can be sealed with 3D-printed small plugs. Finally, small dosimeters can be placed in a variant insert below the inner organs (also shown in figure 3), thus enabling a flexible and independent adaptation of each object.

2.2.3. Material choice

As a second step, we chose appropriate AM materials for CT based on our previous work, during which we analysed five different AM processes with sixteen different printing materials (Wegner *et al* 2020). These AM procedures comprised powder bed, light polymerization, and material extrusion processes. The analysis was performed at a clinical CT device for radiation treatment planning (Siemens Somatom Definition AS (Siemens Healthcare GmbH, Erlangen, GER)) with a voltage of 80 kV, a tube current of 32 mA, and a spatial resolution of 0.6 mm. We investigated both the x-ray absorption properties and printing spatial resolution, together with production costs, availability, and type of printer. Using the known HU-to-electron-density calibration curve, we also estimated the mass density of the printed materials.

The final materials and printing processes are summarized in table 1. We manufactured the body of the first phantom family with the clear resin from the Formlabs SLA-printer 'Form2+' (Formlabs Inc., Sumerville, MA). Although its average CT number is higher than those of soft tissue, this material is characterized by a high printing resolution and offers high accuracy for creating organ cavities. These cavities, corresponding to the relevant organs, were filled with a gypsum-water mixture (bones), an agarose-water mixture (brain, gastro-intestinal tract, kidney), and water (testicles, bladder), respectively. To ensure a satisfactory bone representation, we used a high-frequency vibrating table (FORM + TEST Seidner&Co. GmbH, Riedlingen, GER) for spreading the gypsum, and added water with a fine hollow needle. In the same way, we can fill up other organs with liquids or agarose mixtures. While it is not necessary to seal up the cavities containing gypsum and agarose mixtures, we left very small holes to fill up bladder and testicles (see figure 2(c)). The very thin opening for filling up these cavities with water is designed in such a way that the liquid cannot easily evaporate or spill out. Lungs and ear canals were left empty as a first approximation. We could observe that, by keeping the phantom refrigerated and inside a water-tight box, the agarose mixture inside the organ cavities is stable, in shape and volume, for three days, then the mixture can be removed and the cavities refilled.

For the second phantom family, we chose the same material and procedure as above for the body and inner organ shells, while the plugs were printed with the flexible material from the Formlabs SLA-printer 'Form2+'. Also in this case, the skeleton material, a glass-filled fine polyamide (PA3200 GF in table 1), printed with the Formiga P110 by EOS (EOS GmbH, Krailling, GER), was chosen due to immediate availability. The same

Table 1. Properties of the AM materials chosen to manufacture the phantoms during this work, together with respective printing resolution (Spallek *et al* 2016, Wegner *et al* 2020). Sample volume: 1.37 cm^3. The analysis was carried out at a clinical CT, as described in section 2.1. The material density after printing as provided by the manufacturers is also shown.

AM process	Printer	Material	Printing resolution (μm)	CT values (HU)	Mass density from manufacturer (g cm^{-3})	Mass density from CT calibration (g cm^{-3})
Stereolithography	Formlabs Form2+	Clear resin	50	106 ± 61	1.11 ± 0.03	1.1 ± 0.5
Stereolithography	Formlabs Form2+	Flexible resin	50	154 ± 36	1.07 ± 0.03	1.1 ± 0.3
Laser sintering	EOS Formiga P110	Glass-filled polyamide (PA3200 GF)	100	490 ± 53	1.27 ± 0.03	1.3 ± 0.1

Table 2. Phantom irradiation protocols used in this work. If not specified, the used field had a rectangular shape.

Treatment volume	Radiation quality	No. of fields	Field configuration	Field size	Prescription depth (mm)	Prescribed dose (Gy)
Brain	6 MV	2	Ventro-dorsal, MLC	$36 \times 15\ mm^2$	5.0	2.0
Lungs	6 MV	4	Four-field box, MLC	$40 \times 27\ mm^2$, $36 \times 27\ mm^2$	8.0	2.0
Abdomen	6 MV	2	Ventro-dorsal	$20 \times 20\ mm^2$	10.0	2.0
Whole body	6 MV	2	Ventro-dorsal	$92 \times 44\ mm^2$	12.0	2.0
Brain	200 kV	1	Dorsal	$10 \times 10\ mm^2$	0	3.0
Abdomen	200 kV	1	Dorsal	$10 \times 20\ mm^2$	0	3.0

agarose-water mixture is used as for the first concept to fill the inner organs. After assembly, we investigated the use of olive oil (as fat surrogate) to fill the body from the top filling hole. Due to the viscosity of the oil and an inner barrier in the model shell, the model is leakproof.

2.3. Characterization of phantoms for CT imaging

After printing, we filled both phantoms with tissue equivalent material mixtures, where necessary (figures 2 and 3), and scanned with the above-mentioned clinical CT and a micro-CT (Scanco Medical System, model VivaCT 80, Zürich, CH) for analysing the x-ray contrast properties and the phantom quality. Also, we measured the CT numbers in Hounsfield Units (HU) by means of the clinical CT and the linear attenuation coefficients at the micro-CT (effective filter: 0.5 mm Al). For both devices, we selected a tube voltage of 70 kV. The scanning spatial resolutions were 0.6 mm and 39 μm, respectively.

2.4. Phantom use for quality assurance in radiation therapy

2.4.1. Irradiation geometries and qualities

We performed irradiations with both megavoltage and kilovoltage photons. For megavoltage photons (6 MV), we used a medical linear accelerator for stereotactic dose delivery (TrueBeam™ STx, Varian Medical Systems Inc, Palo Alto, CA). For positioning the phantoms on the patient's treatment couch, we prepared a thermoplastic structure, which could be fixed onto a mask support. We irradiated several target volumes by using different field configurations and, in some cases, by forming the irradiation fields with the multi-leaf collimator (MLC), as shown in table 2. For kilovoltage photons, we used an orthovoltage x-ray tube, which was adapted for mouse irradiations (figure 5(b)). This x-ray tube has a voltage of 200 kV, a current of 20 mA, and a filter of 0.5 mm Cu (additional filter: Be exit window, 7 mm in thickness). The tube is equipped with primary collimators, made of stainless-steel and MCP 96, and a stainless-steel collimation tube (height: 100 mm, width: 100 mm at 300 mm from the x-ray source). A secondary collimation, obtained with 10 mm thick, custom-made MCP 96 blocks, provides quadratic and rectangular field sizes between (10×10) and $(80 \times 80)\ mm^2$. Their dosimetric properties were characterized in a previous work in terms of dose to water traceable to primary standards (Frenzel *et al* 2014), so that look-up tables are available for each field size. Also in this case, we delivered dose to several target volumes (see table 2) with a single dorsal field after fixing the phantom to the mouse treatment couch. Due to limited availability of field sizes, we could not irradiate the whole body with kilovoltage photons.

2.4.2. Dose calculations

We planned linac-based treatments with *Eclipse*™ (Varian Medical Systems Inc, Palo Alto, CA) after manual contouring of target volumes and relevant organs on clinical CT images of the phantoms. The planned dose was calculated with a spatial resolution of 1 mm. Treatment was planned and delivered with additional bolus material (10 mm in thickness) for reducing dose build-up effects. Some examples of target volume definition, field set-up, and beam-eye's views can be seen in figure 4.

For the orthovoltage x-ray tube, which well represents radiation qualities commonly used for small-animal irradiations, we developed a Monte-Carlo model using GATE, version 8.2 (Jan et al 2016, Camarasu-Pop *et al* 2013, Sarrut *et al* 2014). We run the simulations with the Livermore physics model, implemented in Geant4, version 10.5.1, which describes the interactions of electrons and photons with matter down to about 250 eV using interpolated data tables based on the Livermore library (EADL-EEDL-EPDL) (https://www-nds.iaea.org/epdl97/). In a first step, the simulation transports a pencil beam of mono-energetic electrons with 200 keV kinetic energy impinging on the tungsten anode (angle: 20°) and the produced x-rays are transported through the Be exit window, the Cu filter, and the primary collimator. The orthovoltage x-ray tube used for this study was

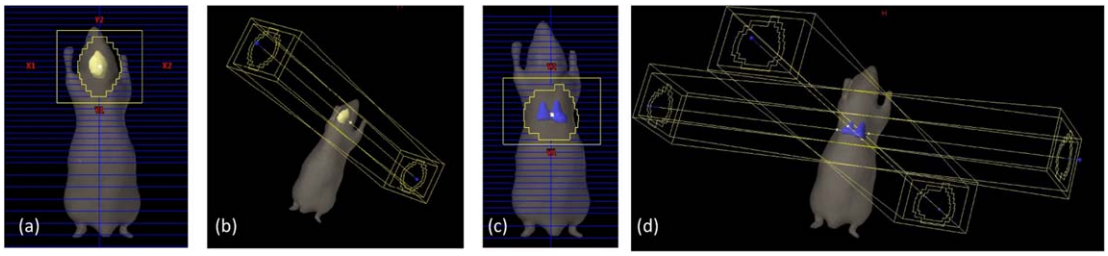

Figure 4. Examples of field set-up, beam-eye's view, and organ segmentation in the irradiation treatment plans for C1 in Eclipse. The brain is highlighted in yellow for a brain beam-eye's view and the field set-up, respectively (a), (b), while the lung is highlighted in blue (c), (d).

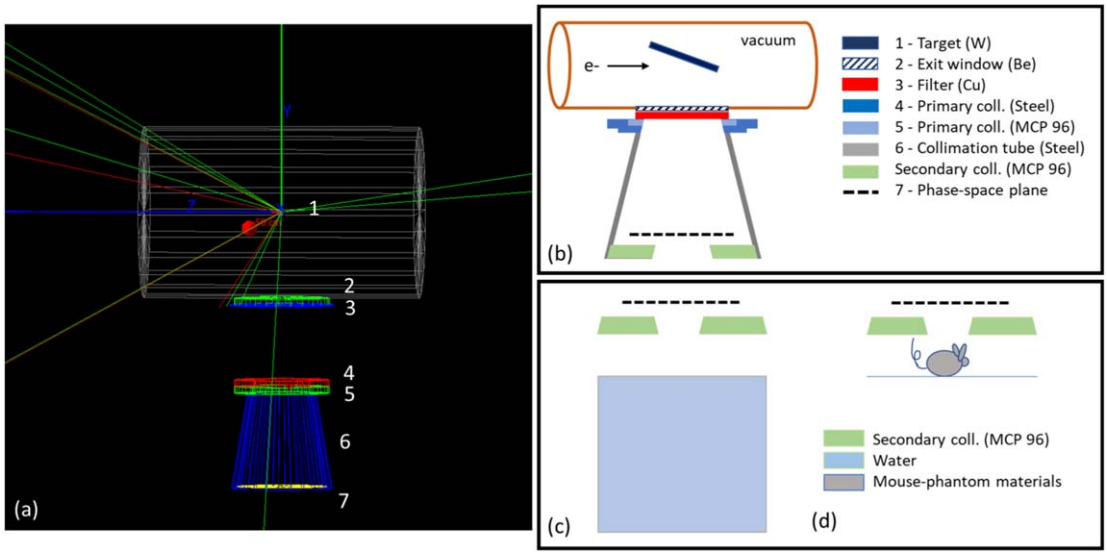

Figure 5. Schematic representation of the x-ray facility that was used in this work, with all relevant materials, as implemented in the Monte Carlo code GATE (a). The drawing (adapted from Frenzel *et al* (2014)) is not to scale (b). The orange cylinder represents the x-ray tube, in which a pencil beam of mono-energetic electrons in vacuum impinges on a tungsten target. The GATE geometry excludes the secondary collimators (in green) in the first step. These are used in a second step to verify and calibrate the model in a water phantom (c) and to calculate the dose in the mouse phantom C1 (d). The dashed line represents the position of the phase-space plane above the secondary collimator (b–d).

simulated as shown in figures 5(a) and (b). The source phase-space file was recorded on a plane located 2 mm above the secondary collimator, so that, in a second step, we could simulate the x-ray transport of collimated beams starting from this plane (see figures 5(a) and (b)).

To verify the Monte Carlo model, we calculated percentage depth-dose curves (PDD) and dose profiles in water for several field sizes and compared them to the experimental data (figure 5(c)). The spatial resolution of the dose calculation in a water phantom, 15 cm in size, was 1 mm. Furthermore, we compared the absolute dose on the field central axis at 4 mm depth. This is the point at which the dose output factors were previously determined (Frenzel *et al* 2014).

In a further step, we simulated phantom irradiations for C1 by including the phantom volume model, shown in figure 1, in the simulation and starting the photons from the phase-space plane, as schematically illustrated in figure 5(d).

We implemented the phantom material composition according to nominal data found in the literature (see table 3). As a further verification of this implementation, we determined a priori the corresponding linear attenuation coefficients and relative electron densities. The linear attenuation coefficients were retrieved from the NIST XCOM database (https://physics.nist.gov/cgi-bin/Xcom) and are shown in figure 6, together with other relevant materials for comparison, including human tissues. We also retrieved these coefficients for the mean energy of the x-ray spectrum (19.5 keV) of the micro-CT scanner with the above-mentioned scanning parameters, so that we could later compare with measured data. We calculated the mean energy of the spectrum with SpekCalc (Poludniowski 2007, Poludniowski and Evans 2007, Poludniowski *et al* 2009). Finally, for a comparison with the data from the clinical CT images, we also calculated the relative electron densities (ρ_e):

Table 3. Properties of the materials used for the Monte Carlo simulation. The composition for mixtures is expressed as weight percentage. The relative electron density was calculated with equations (1) and (2). The NIST linear attenuation coefficient was retrieved from the NIST XCOM database for a photon energy 19.5 keV, which corresponds to the mean x-ray spectrum of the micro-CT scanner used in this work. Due to lack of exact information from the manufacturer, we approximated clear resin with Methyl Metachrylate.

Material	Density (g cm^{-3})	Composition (weight percentage)	Relative electron density from equation (1)	NIST linear attenuation coefficient for 19.5 keV (cm^{-1})
Clear resin (surrounding tissue)	1.09	$C_5H_8O_2$ (Methyl Metachrylate)	1.06	0.318
Gypsum-water mixture (skeleton)	1.2	$CaSO_4$ (98%), H_2O (2%)	1.08	1.974
Agarose-water mixture (inner organs)	1.02	$C_{10}H_{15}N_3O_3$ (5%), H_2O (95%)	1.02	0.35

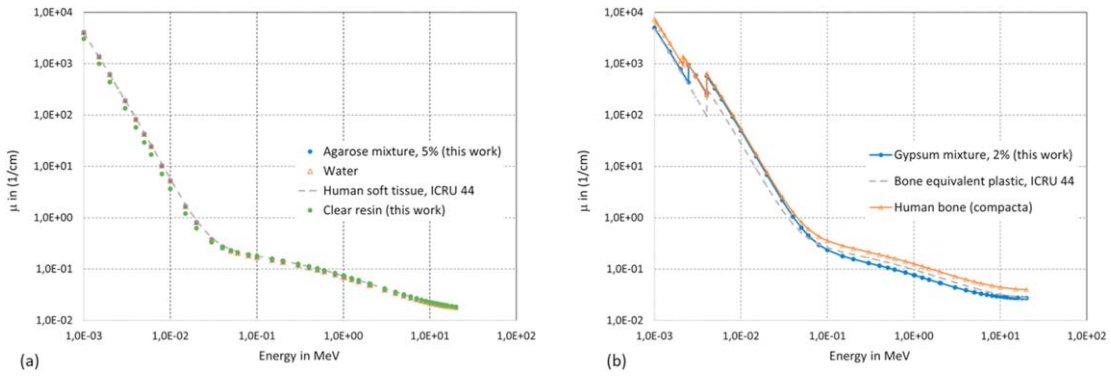

Figure 6. Linear attenuation coefficients for the surrogates used in this work, together with human tissue-equivalent materials (a) and bone-equivalent materials (b), retrieved from the NIST XCOM database (https://physics.nist.gov/cgi-bin/Xcom). For the materials used in this work, we retrieved the data using composition and densities as listed in table 3.

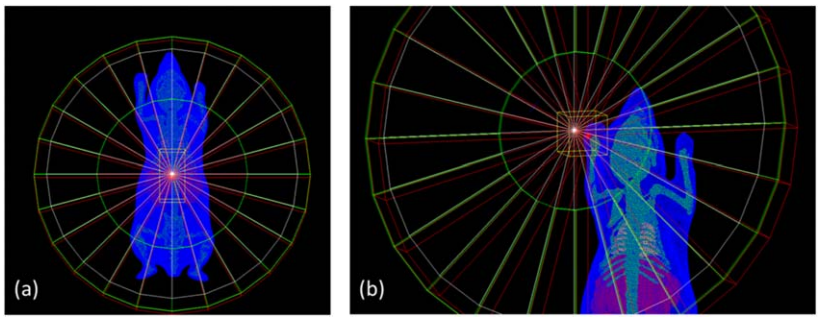

Figure 7. Mouse-phantom irradiation geometry implemented in GATE. Front view of an irradiation of the abdomen (a) and prospective view of an irradiation of the brain (b). The aperture of the secondary collimator is shown in yellow. The lower part of the collimation tube is drawn in red. The photons stored in the phase-space file start from the white plane. For variance reduction, a circular area (in green) is defined to kill scattered particles.

$$\rho_e = \rho \cdot N_A \cdot Z/A, \tag{1}$$

where ρ is the mass density, N_A the Avogadro's constant, and

$$Z/A = \sum_i w_i \cdot (Z/A)_i. \tag{2}$$

being w_i the fraction by weight of each element in the material.

The final geometry for the simulation of mouse irradiations with GATE when starting the particles from the phase-space plane is depicted in figure 7. Also in this case, the spatial resolution of the dose calculation grid is 1 mm. The material properties are implemented in the GATE material database as indicated in table 3.

2.4.3. Dose measurements

The printing of different phantom variants for C1 allows for measurements with different available dosimeters (see figures 2(d)–(f)). Both at the linac and at the mouse-irradiation facility, for the irradiation protocols reported in table 2, we measured two-dimensional dose distributions with radiochromic films (Grafchromic EBT3, Ashland, Covington, KY) (figure 3(a)). The films were positioned in the mouse phantom as shown in figure 2(d) and calibrated in the range between 150 mGy and 3.5 Gy in terms of dose to water. For calibration and evaluation, we scanned the films with an Epson Expression 10000XL flatbed scanner (Seiko Epson K.K, Suwa, Japan) 24 h after irradiation and then analysed them with the software *SNC-Patient* (Sun Nuclear Corporation, Melbourne, FL). For the second phantom model (C2), we also performed dose measurements at the linac, in the abdominal region, with radiochromic films.

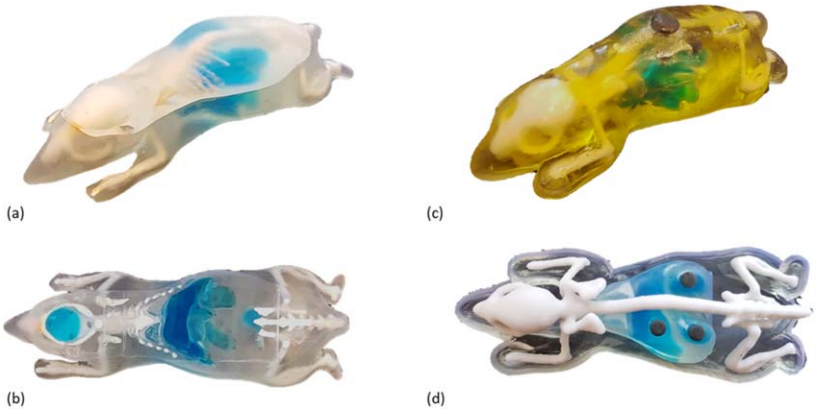

Figure 8. View of the two manufactured phantoms. Concept 1 (a)–(b), Concept 2 (c)–(d). Details of the lower part of C1 (b) and inner parts of C2 (d) can also be seen. The colours were chosen for a better visualisation.

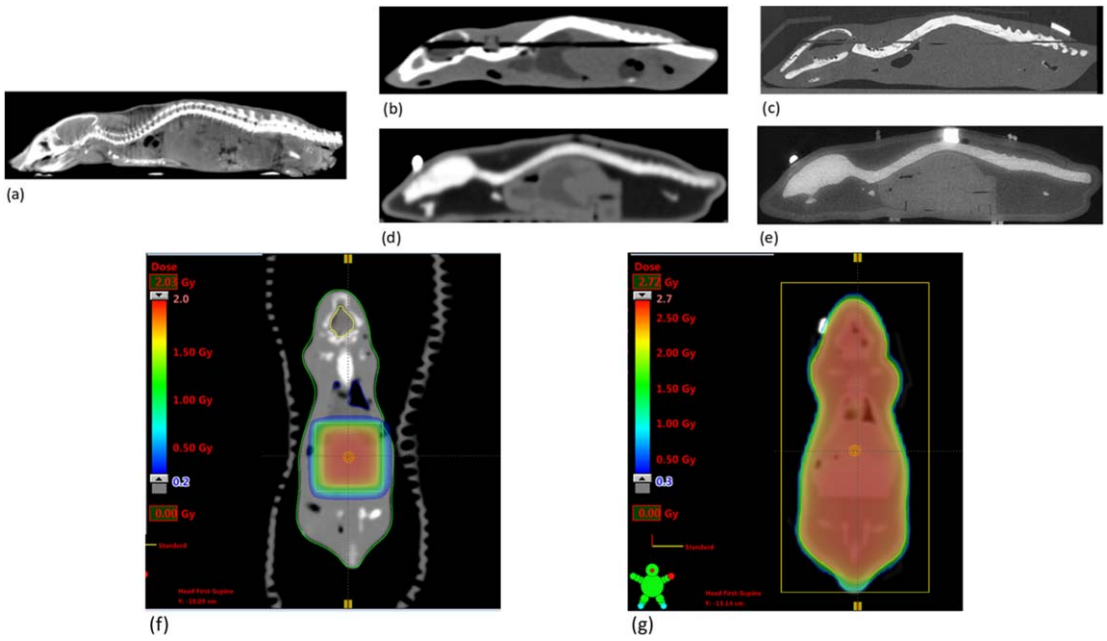

Figure 9. Comparison between real mouse (a) and phantom images (b)–(e). The real mouse was scanned by Dogdas *et al* (2007) for building the Digimouse atlas. (b, c) CT-and micro-CT-image of C1. (d,e) CT-and micro-CT-image of C2. In some images (c), (d), (e), positioning markers are visible. The comparison is only qualitative. CT-based dose distribution in Eclipse, represented as colour wash (f), (g). Abdomen irradiation for C1 (f) and total body irradiation for C2 (g). The yellow rectangle represents the field shape.

3. Results

3.1. Analysis of CT contrast and material homogeneity of the two phantom concepts

Figure 8 shows the two manufactured phantoms with cavities filled up with different mixtures, while CT images of both models can be observed in figure 9, together with the original micro-CT image of the *Digimouse* atlas.

From a qualitative point of view, the clear resin used for building C1 is characterized by an excellent homogeneity and spatial resolution, while the gypsum filling shows some small heterogeneities but very good x-ray contrast properties. Also, the agarose mixture results to be mostly homogeneous and is clearly visible in the clinical CT scan, but offers a too low contrast with respect to the clear resin in the micro-CT images. Water cannot be distinguished from the clear resin in the micro-CT images but, as expected, gives adequate contrast in the clinical CT images. The latter present some artefacts in the area of the coronal cut between the two phantom parts of the first model and in the presence of small air enclosures. These artefacts are negligible in the micro-CT images due to the higher spatial resolution. Moreover, olive oil is an adequate fat surrogate and creates contrasts with the skeleton of the second model. Finally, the glass-filled fine polyamide considered for C2 can be used as

Table 4. Linear attenuation coefficients measured at the Micro-CT (voltage: 70 kV, filter: 0.5 mm Al, mean x-ray energy: 19.5 keV) for both phantoms and a real mouse in regions with a volume of 1.5 mm^3. The data for the mouse was not acquired during this work but was available at the same device and obtained with the same scanning protocols used in this work for the phantoms.

Mouse		Concept 1		Concept 2	
Tissue	Linear attenuation coefficient (cm^{-1})	Material	Linear attenuation coefficient (cm^{-1})	Material	Linear attenuation coefficient (cm^{-1})
Adipose tissue	0.39 ± 0.17			Olive oil	0.31 ± 0.17
Lung tissue	0.14 ± 0.18	Air	-0.02 ± 0.15	Air	-0.03 ± 0.16
Bone (compacta) Bone (spongiosa)	2.91 ± 0.1 0.91 ± 0.27	Gypsum	1.9 ± 0.34	Glass-filled polyamide	0.91 ± 0.27
Soft tissue	0.53 ± 0.16	Agarose mixture	0.48 ± 0.14	Agarose mixture	0.48 ± 0.16
		Clear resin	0.45 ± 0.16	Clear resin	0.46 ± 0.18

bone-mimicking tissue with satisfactory results. However, since the printing resolution, as stated in table 1, is lower, the manufactured skull consists, in this case, of full material, as can be observed in figures 9(d) and (e).

The CT numbers of the different phantom materials, which were measured at the clinical CT in regions with a volume of 1.5 mm^3, resulted to be close to typical values for biological tissues. For example, for olive oil, used for adipose tissue, we measured (-142 ± 5) HU, while the agarose mixture produced (27 ± 3) HU (CT numbers of printed materials listed in table 1). For a more specific comparison with mouse tissue, we measured the linear attenuation coefficients of the phantom materials at the micro-CT and compared them with those of a real mouse that was investigated with the same scanner and scanning parameters. The corresponding results are listed in table 4 and show that the linear attenuation coefficients of the two surrogates for soft tissue (clear resin and agarose mixture) are smaller than that measured for the living mouse (by about 15%). This difference is much larger for gypsum as the bone surrogate. In fact, the linear attenuation coefficient of the gypsum mixture is about 35% smaller than that of bone compacta and almost a factor of two larger than the coefficient of bone spongiosa of the mouse. On the other hand, the glass-filled polyamide well represents bone spongiosa, with equal linear attenuation coefficients (within the experimental uncertainties). A closer look to the theoretical values estimated in table 3 for these surrogates demonstrates a good agreement with the experimental ones for gypsum, with a deviation of about 4% (theoretical estimation: 1.974 cm^{-1}), but an underestimation by approximately 30% for those of clear resin (theoretical estimation: 0.318 cm^{-1}) and the agarose mixture (theoretical estimation: 0.35 cm^{-1}). The relative difference between the attenuation coefficients for mouse adipose tissue and olive oil as the fat surrogate is about 20%.

3.2. Dose calculations

3.2.1. Linac irradiations

Figures 9(f) and (g) show, as an example, the CT-based dose distribution in the coronal plane calculated with Eclipse for phantom irradiations with 6 MV photons for the abdomen (C1) and the whole body (C2) as target volumes.

3.2.2. x-ray tube irradiations

A simulation of 8×10^{10} primary electrons resulted in the creation of a phase-space file with 3.4×10^8 photons. Therefore, when starting photons from this phase-space file, the dose per photon needs to be multiplied by:

$$K = 5.31 \times 10^{14} \text{particles (mA s)}^{-1}.$$

Using the same phase-space file, we also obtained PDDs and dose profiles at 4 mm, for comparison with the previous experimental work (Frenzel *et al* 2014). For reducing the statistical uncertainty to approximately $\pm 2\%$, we simulated between 3×10^9 and 4.5×10^9 photons, depending on the field size. As an example, we report these curves for two field sizes in figure 10, together with the corresponding experimental data.

3.3. Dose measurements

In figures 11(a)–(c) we demonstrate how the lower part of phantom C1 was adapted to place different dosimeters, while details concerning the phantom positioning during the experiments can be seen in figures 11(d) and (e). As mentioned in section 2.4.2, we prepared CT-based radiation treatment plans for dose delivery at the linac and used look-up tables for dose delivery at the x-ray tube.

Unlike for linac irradiations, we did not have any image-based positioning check at the x-ray tube. We therefore present here the dose measurements with films, only, so that we have a consistent and more detailed comparison with calculations for both radiation qualities. Table 5 reports the experimental and calculated dose

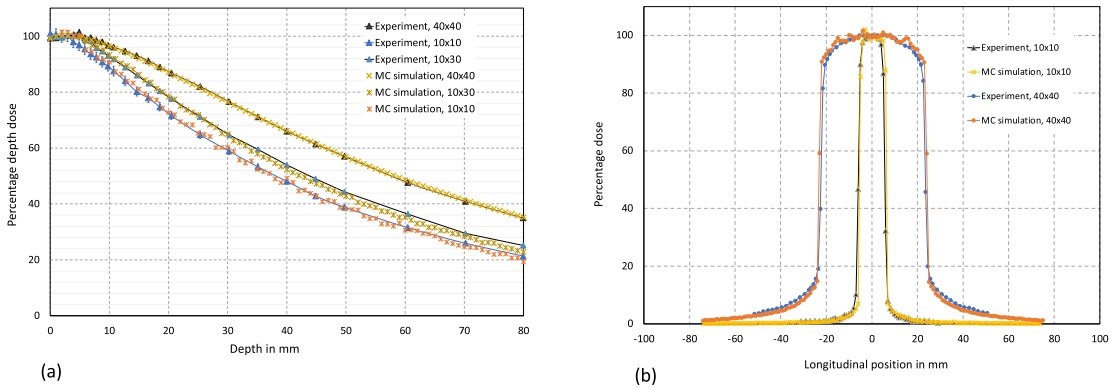

Figure 10. Comparison of PDDs (a) and longitudinal profiles at a depth of 4 mm (b) in water for validating the Monte Carlo simulation model of the x-ray tube. For the sake of simplicity, we show here only a few field sizes. The experimental data were obtained in a previous work (Frenzel *et al* 2014). The MC simulations were performed with GATE. See text for more details. The maximum relative statistical uncertainty (1σ) for the MC simulated data was $\pm 2.5\%$.

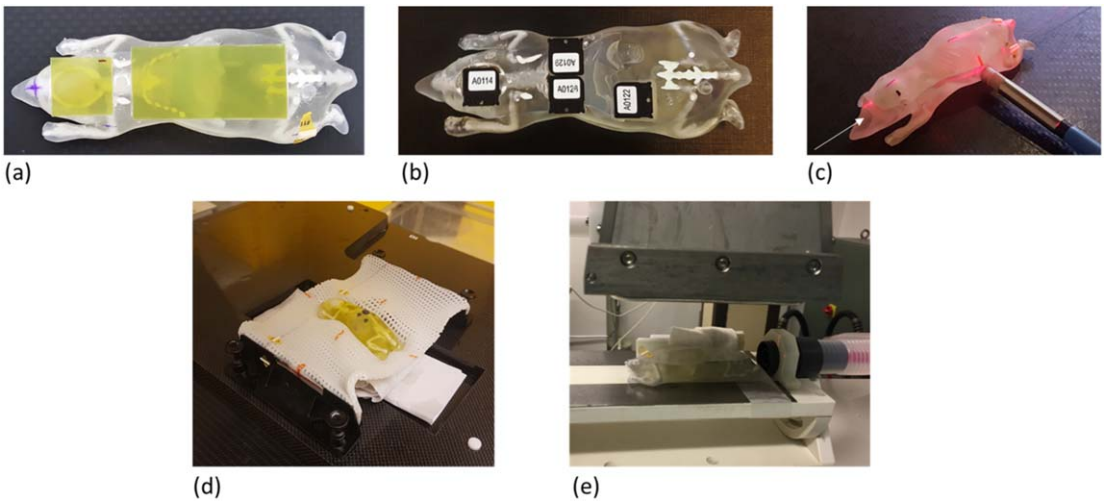

Figure 11. Example of dosimeter placement in the printed phantom (C1). Radiochromic films (a) are be placed in areas corresponding to brain and abdominal regions at a depth of approx. 4 and 12 mm, respectively. OSL dosimeters (b) are set to measure point dose in brain, lungs and kidney. The ion chamber (c) can be inserted in the abdominal region, as well as in the head (green arrow). Reproducibility of phantom positioning prior to irradiation: (d) on the linac couch, by means of a thermoplastic bed (C2) and (e) on the mouse irradiation bed (collimator-to-bed distance = 5 cm) at the orthovoltage x-ray tube (C1).

Table 5. Results of film dosimetry for phantom Concept 1 (C1) and Concept 2 (C2) after irradiation of the mouse phantom according to the protocols from table 2. The dose was calculated with Eclipse for 6 MV and with GATE for 200 kV. We report the mean dose (with standard deviation) at the centre of the target volume, at the given depth, within a region of interest of (2×2) mm^2.

Phantom concept	Radiation quality	Treatment volume	Depth in phantom (mm)	Measured dose (mGy)	Calculated dose (mGy)	Relative deviation (%)
C1	6 MV	Brain	4	2113 ± 63	2069 ± 2	2.1
C1	6 MV	Lungs	7	2157 ± 65	2181 ± 1	1.1
C1	6 MV	Abdomen	12	1885 ± 57	1878 ± 28	0.4
C1	6 MV	Whole body	4	1855 ± 56	1928 ± 3	3.8
			12	1980 ± 59	1992 ± 4	0.6
C1	200 kV	Brain	4	3140 ± 50	3520 ± 250	12.0
C1	200 kV	Abdomen	12	3200 ± 84	3310 ± 110	3.4
C2	6 MV	Whole body	15	2567 ± 77	2590 ± 3	0.4

at the centre of the target volume. For better accuracy, we evaluated a 2 mm square region. The observed relative deviation between planned and measured values lies within $\pm 4\%$, except for the brain irradiation at the small-animal x-ray tube.

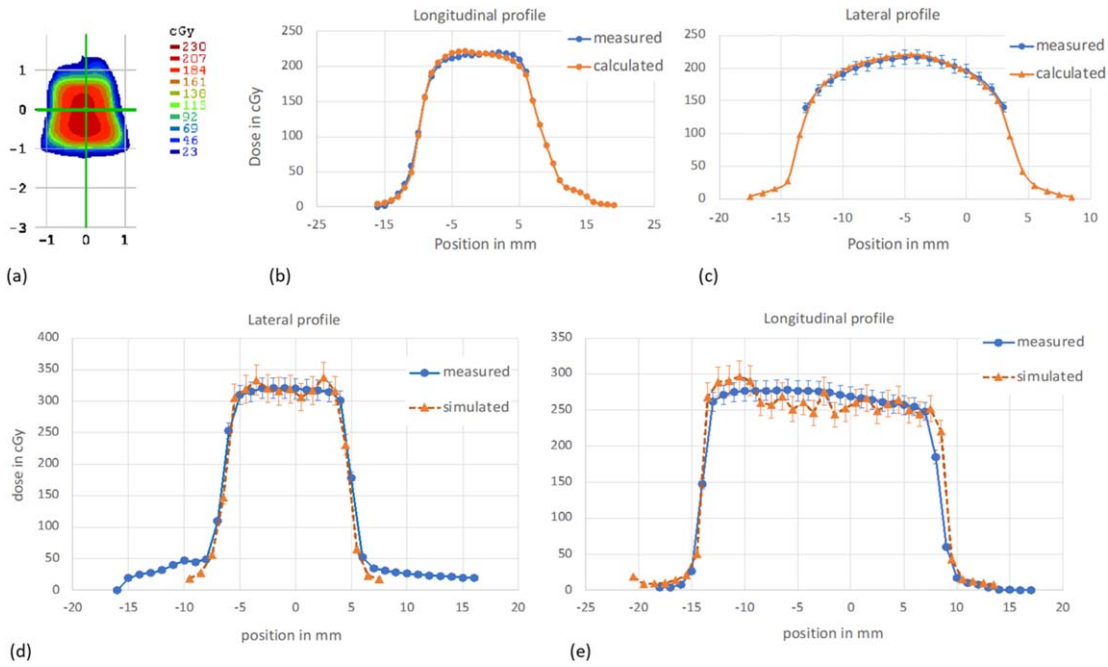

Figure 12. Example of calculated 2D dose distribution in the coronal plane (a), together with the longitudinal and lateral profiles (b,c) along the two green lines in (a) for the lung irradiation of C1 at the linac according to the protocol mentioned in table 2. The orange curves were obtained with Eclipse, the blue curves measured with Gafchromic films. The error bars represent the overall uncertainty of film dosimetry (± 5%). Example of lateral (d) and longitudinal profile (e) for the abdomen irradiation of C1 with the x-ray tube according to the protocol mentioned in table 2 (field size: 10 × 20 mm^2). The profiles were analysed along the central axis. The error bars for the Monte Carlo simulated data show the relative statistical uncertainty (1σ, ± 6%), while those for the measured profiles represent the overall uncertainty of film dosimetry (± 5%).

The dose profiles along the central axis for the lung plan of C1 (s. Table 2) show how well the values of measured and planned isodose lines correlate (figures 12(b)–(c)), with a maximum discrepancy of 3.5% in the dose gradient. The calculated and simulated lateral and longitudinal profiles for the x-ray tube, as can be seen in figures 12(d) and (e), agree, in general within less than ±5%, with higher discrepancies (maximum: ± 10%), in regions along the spinal cord.

4. Discussion and conclusion

During this work, we designed, produced, and characterized two modular, anatomically accurate mouse phantom prototypes, which are multi-purpose and, therefore, suitable for quality assurance and training at small-animal irradiation devices, and can be printed in about four hours. The costs for printing material and surrogate material are about 25€ per phantom, without considering electricity costs and labour time. We obtained the volume model from a freely available mouse atlas (*Digimouse* is available online at: https://neuroimage.usc.edu/neuro/Digimouse). Moreover, it is possible to create or edit the STL-files using open-source software (*3D Slicer*, available at: https://www.slicer.org; *Autodesk Meshmixer*, available at: https://meshmixer.com), so that no additional costs arise from software. Users without access to stereolithography printers, can order the phantom modules from several private 3D-printing services. In this case, the total costs for one phantom would be below 100€. The phantom STL-files used can be made available for download from the corresponding author upon request.

The use of mouse phantoms in radiobiology research could also reduce the use of living animals, or cause them less stress, for example by carefully designing new irradiation protocols prior to use in research. Both phantoms contain adjustable bone, lung, and organ cavities, which can be easily adapted and custom filled with simple and inexpensive tissue-surrogate mixtures. For example, organs can be added or deleted, and flexible printing materials (such as the flexible material from the Formlabs SLA-printer 'Form2+' mentioned in table 1) can be used in the future to simulate organ changes (such as bladder filling). Moreover, these phantoms are provided with inserts for different dose-measuring systems, which, also, can be adjusted for specific needs.

In addition to showing adequate anatomical details and tissue contrast for clinical CT and micro-CT imaging, the linear attenuation coefficients of the current materials are, at least for the imaging spectra considered in this study, close to those of mouse tissues, with the only exception of bones. In fact, the actual

water-gypsum surrogate is too radiologically dense to represent bone spongiosa and not dense enough for bone compacta. For this reason, the surrogate composition for bone should be improved in the future. Also, we did not implement any tissue surrogate for lungs and left them void. The same approach was used by Price *et al* (2020) and, at least for radiation qualities that are commonly used for small-animal irradiations, we do not expect large deviations of the dose in the surrounding region, due to the small lung volume and CT numbers close to those of air. However, this difference might result to be significant when irradiating with lower photon energies. As also recommended by Price *et al* (2020), surrogates for lung tissue will be investigated in future work.

The phantoms can be used for dose verification, both at a linear accelerator and at common x-ray tubes. In fact, we could perform CT-based dose calculations for several body regions using the clinical treatment planning system. Also, we could carry out first Monte Carlo simulations implementing the phantom in the irradiation geometry. The STL-files of the single components, which are based on the original 3D model and created for additive manufacturing, can be directly imported as volumes into GATE and be assigned nominal material properties. Calculations and experimental data agree within less than $\pm 4\%$ for CT-based irradiations at the linac, while some larger deviations can be seen for x-ray treatments, especially in the presence of bones, with a maximum discrepancy of about $\pm 12\%$ in the brain, with a larger simulated dose.

The results of our comparisons between measured and calculated dose are similar to other published data. For example, Esplen *et al* (2019a, 2019b), who manufactured their phantom with AM using PMMA-like materials, obtained an agreement within less than $\pm 5\%$ between simulated dose and 2D film measurements, while Soultanidis et *al* (2019) reported discrepancies below $\pm 2\%$ between calculated and alanine point dose measurements. Based on the reported information by both group, material composition of their mouse phantom is known with a higher accuracy, especially for boney structures.

The discrepancies between measured and simulated dose observed in this study are mainly due to the fact that the material compositions implemented in the Monte Carlo simulation do not perfectly match the real composition. Due to the relatively low mean x-ray energy of the tube considered in this study (about 94 keV), the role of photoelectric absorption plays a more important role than in the case of irradiations at the linac, thus requiring a much better analysis of the surrogate compositions for future applications. As shown in figure 6, the linear attenuation coefficients of the considered water-gypsum mixture are, on the one hand, comparable to those of human compacta bone in the energy range between 10 and 60 keV. On the other hand, we can observe larger deviations for higher energies. When comparing to the ICRU-44 bone-equivalent plastic (ICRU 1989), the linear attenuation coefficient of our mixture is systematically lower over the whole energy range. Even though it was demonstrated that murine tissue differs, in composition and density, from that of humans (Schyns *et al* 2019), it is a common practice to use human tissue composition for dose calculation in mice. We can therefore conclude that this surrogate might be used also for lower irradiation energies. In the range of soft tissue, figure 6 shows that clear resin, the proposed agarose mixture, and water have linear attenuation coefficients that are good in agreement with that of ICRU-44 soft tissue for x-ray energies above about 30 keV, while the coefficient for clear resin is systematically lower than that of the other materials for lower energies, which is in agreement with the results of table 4. Thus, for irradiations with softer spectra, it might be possible that a larger deviation between Monte Carlo simulations and experiments is observed. All in all, the acquisition of more accurate data on our tissue surrogates, especially composition and density, will be aimed for in future work.

Despite some limitations, mostly caused by incomplete information on surrogate elemental compositions, which increases the uncertainty in the dose calculation, the presented methodology contains some novelties with respect to past mouse phantom development work. In fact, for the first time, we show that it is possible to spread multi-purpose and cost-effective mouse phantoms in the small-animal irradiation community by downloading the STL files and print them with low material costs and open-source 3D printing software. The costs remain affordable also for users without stereolithography printers since the online offer of 3D printing services have increased significantly.

This novel approach brings standardization of quality assurance in small-animal irradiation a step forward. In fact, (i) training and the introduction of new irradiation techniques can be realised in a more efficient way, since workflow testing and reproducibility analysis do not harm animals; (ii) the effect of different parameters, like animal positioning uncertainties, or changes in imaging protocols, can be easily quantified, independent of the accuracy of dose calculations; (iii) the flexible positioning of different types of dosimeters makes the use of these phantoms accessible to any radiobiology lab, provided that standard dosimetry protocols are implemented.

As already pointed out by Schyns *et al* (2019), the current Monte Carlo based dose calculation methods in small-animal irradiations rely on reference data for human tissues, since such data is missing for mice. The group assessed the effective atomic number and the electron density of soft and bone tissues in nine female mice by means of the non-invasive technique of dual-energy CT imaging. Their findings show a large spread of these values, depending on the considered tissue. The authors also demonstrated that the use of reference human

tissue parameters can introduce large errors to dose calculations in a mouse. For orthovoltage x-ray beams, this error could be as large as 20% in bone tissue. Without the use of a treatment plan (as in our case for the exposures at the orthovoltage x-ray machine), dose prescription is usually defined in terms of dose to water, according to standard dosimetry protocols. Therefore, also in this case, the delivered dose might significantly differ from the expected dose. A way to quantify these differences would be to perform *in vivo* dosimetry for a variety of cases.

The study of Seed *et al* (2016), which was intended as dosimetry intercomparison exercise among seven laboratories in Japan and the USA, showed that the lack of a dosimetry and quality assurance protocol at small animal irradiation facilities is the main cause of large errors in dose delivery to laboratory animals. Interestingly, the authors first asked the participants to embed OSL dosimeters into the abdominal cavity of freshly sacrificed mice and deliver a standard target dose. In four out of seven institutions, the delivered dose differed significantly from the target dose, with a maximum average error of about 22%. These four institutions carried out irradiations with orthovoltage x-ray machines, while the others used ^{137}Cs- or ^{60}Co-irradiators. Concluding that these errors could be caused by the energy dependence of the used OSL dosimeters for low-energy spectra, which was not correctly taken into account, the group developed a second experiment with TLDs. Irradiations, this time, were carried out with homogeneous acrylic phantoms instead of mouse cadavers. Also in this case, in some laboratories the discrepancy between expected and delivered dose was significant. Since the study focused on the question of quality assurance, and due to the fact that the measurements were performed with different 'phantoms' (dead mice versus acrylic, mouse-like cylinders), we cannot draw any conclusion about the effect of heterogeneity or different attenuation properties in mice on delivered dose. Therefore, in the future, it would be interesting to perform a similar study with a consistent experimental set-up and accurate dosimetric characterization of the irradiation devices to exclude other sources of uncertainty.

Instead of using mouse carcasses, compliance with the 3R-philosophy would suggest, however, to manufacture mouse phantoms, as shown in this work. In this case, the phantoms could be printed and filled with surrogates with varying compositions, which could cover the spreads in electron density and effective atomic number that were encountered by Schyns *et al* (2019). This would enable a systematic quantification of the effects of heterogeneities and tissue composition on calculated and delivered dose without sacrificing animals.

As a summary, while the first phantom concept is more flexible for dose measurements and thus more practical for quality assurance, the second concept is designed to be more suitable for multimodal imaging experiments. Future investigations will therefore be performed to establish the use of Concept 2 for MRT, PET or sonography, create a larger material database for both prototypes, and define criteria for their use in multi-modal imaging and theranostics, thus enabling the analysis of image registration procedures and end-to-end testing of the whole radiotherapy workflow.

Acknowledgments

Parts of this work are carried out within the research project 'Innovative Technologies in Cancer Diagnostics and Therapy', funded by the Behörde für Wissenschaft, Forschung und Gleichstellung (BWFG) within the framework of the Landesforschungs-Förderung (LFF) Hamburg (Grant Nr. LFF-GRK 10–2019). The authors would like to thank all involved parties for their funding and support. We are grateful to Sabrina Christiansen (UKE, Department of Radiotherapy and Radio-Oncology) and Michael Horn (University Cancer Center Hamburg) for their valuable help in setting up and carrying out the irradiations at the orthovoltage x-ray tube. We also would like to thank Hiroaki Saito (UKE, Department of Trauma-, Hand- and Reconstructive Surgery, Heisenberg Group for Molecular Skeletal Biology) for helping us with the micro-CT scans. Part of the results presented in this work were achieved using the GateLab application through the Virtual Imaging Platform (http://vip.creatis.insa-lyon.fr/, Glatard *et al* 2013), which uses the resources provided by the biomed virtual organisation of the European Grid Infrastructure (EGI). In particular, EG is grateful to Sorina Pop (CREATIS, Lyon, France) for her technical support in this context.

The work of TF was supported by the Mildred-Scheel Cancer Career Center Hamburg, funded by German Cancer Aid and the Hamburger Krebsgesellschaft.

Data availability statement

All data that support the findings of this study are included within the article (and any supplementary information files).

ORCID iDs

Marie Wegner https://orcid.org/0000-0001-8616-859X
Dieter Krause https://orcid.org/0000-0002-1253-1699
Elisabetta Gargioni https://orcid.org/0000-0002-8204-0609

References

Bentz B Z *et al* 2016a Fabrication and application of heterogeneous printed mouse phantoms for whole animal optical imaging *Appl. Opt.* **55** 280–7
Bentz B Z *et al* 2016b Printed optics: phantoms for quantitative deep tissue fluorescence imaging *Opt. Lett.* **41** 5230–3
Biglin E R *et al* 2019 Preclinical dosimetry: exploring the use of small animal phantoms *Radiat. Oncol.* **14** 134
Camarasu-Pop S *et al* 2013 Monte-Carlo simulation on heterogeneous distributed systems: a computing framework with parallel merging and checkpointing strategies *Future Gener. Comput. Syst.* **29** 728–38
Desrosier M *et al* 2013 The importance of dosimetry standardization in radiobiology *J. Res. Natl Inst. Stand. Technol.* **118** 403–18
Diep P *et al* 2015 Three-dimensional printed optical phantoms with customized absorption and scattering properties *Biomed. Opt. Express* **6** 4212–20
Dogdas B *et al* 2007 Digimouse: a 3D whole body mouse atlas from CT and cryosection data *Phys. Med. Biol.* **52** 577–87
Esplen N *et al* 2019a Technical note: manufacturing of a realistic mouse phantom for dosimetry of radiobiology experiments *Med. Phys.* **46** 1030–6
Esplen N *et al* 2019b Preclinical dose verification using a 3D printed mouse phantom for radiobiology experiments *Med. Phys.* **46** 5294–303
Filippou V and Tsoumpas C 2018 Recent advances on the development of phantoms using 3D printing for imaging with CT, MRI, PET, SPECT and Ultrasound *Med. Phys.* **46** 740–60
Frenzel T *et al* 2014 Partial body irradiation of small laboratory animals with an industrial x-ray tube *Z. Med. Phys.* **24** 352–62
Ghita M *et al* 2019 Integrating small animal irradiators with functional imaging for advanced preclinical radiotherapy research *Cancers* **11** 170
Glatard A *et al* 2013 A Virtual Imaging Platform for multi-modality medical image simulation *IEEE Trans. Med. Imaging* **32** 110–8
Gronberg M P *et al* 2020 A mail audit independet peer review system for dosimetry verification of a small animal irradiator *Radiat. Res.* **193** 341–50
ICRU 1989 *Tissue Substitutes in Radiation Dosimetry and Measurement*ICRU-44 (UN89008762)
Jan S *et al* 2016 GATE V6: a major enhancement of the GATE simulation platform enabling modelling of CT and radiotherapy *Phys. Med. Biol.* **56** 881–901
Pedersen K H *et al* 2016 Radiation biology irradiatior dose verification survey *Radiat. Res.* **185** 163–8
Poludniowski G *et al* 2009 SpekCalc: a program to calculate photon spectra from tungsten anode x-ray tubes *Phys. Med. Biol.* **54** N433
Poludniowski G G 2007 Calculation of x-ray spectra emerging from an x-ray tube. Part II. X-ray production and filtration in x-ray targets *Med. Phys.* **34** 2175–86
Poludniowski G G and Evans P M 2007 Calculation of x-ray spectra emerging from an x-ray tube. Part I. Electron penetration characteristics in x-ray targets *Med. Phys.* **34** 2164–74
Price G J *et al* 2020 An open source heterogeneous 3D printed mouse phantom utilising a novel bone representative thermoplastic *Phys. Med. Biol.* **65** 10NT02
Russell W M S and Burch R L 1959 *The Principles of Humane Experimental Technique* (London: Methuen) Record no. 19592204037
Sarrut D *et al* 2014 A review of the use and potential of the GATE Monte Carlo simulation code for radiation therapy and dosimetry applications *Med. Phys.* **41** 064301
Schyns L E *et al* 2019 Murine vs human tissue compositions: implications of using human tissue compositions for photon energy absorption in mice *Br. J. Radiol.* **92** 20180454
Seed T M *et al* 2016 An interlaboratory comparison of dosimetry for a multi-institutional radiobiological research project: observations, problems, solutions and lessons learned *Int. J. Radiat. Biol.* **92** 59–70
Silvestre Patallo I *et al* 2020 Development and implementation of an end-to-end test for absolute dose verification of small animal preclinical irradiation research platforms *Int. J. Radiation Oncol. Biol. Phys.* **107** 587–96
Soultanidis G *et al* 2019 Development of an anatomically correct mouse phantom for dosimetry measurement in small animal radiotherapy research *Phys. Med. Biol.* **64** 12NT02
Spallek J *et al* 2016 Comparing technologies of additive manufacturing for the development of vascular models *Fraunhofer Direct Digital Manufacturing Conf. DDMC 2016*978-3-8396-1001-5
Tino R *et al* 2019 A systematic review on 3D-printed imaging and dosimetry phantoms in radiation therapy *Technol. Cancer. Res. T.* **18** 1–14
Ventola C L 2014 Medical applications for 3D printing: current and projected uses *Pharm.Ther.* **39** 704–11 PMID: 25336867; PMCID: PMC4189697
Verhaegen F *et al* 2018 ESTRO ACROP: Technology for precision small animal radiotherapy research: Optimal use and challenges *Radiother. Oncol.* **126** 471–8
Wegner M *et al* 2020 Comparing technologies of additive manufacturing for the development of modular dosimetry phantoms in radiation therapy *Trans. AMMM* **2** 028
Wegner M *et al* 2021 Einsatzmöglichkeiten der additiven Fertigung in der Herstellung von Phantomen *Konstruktion für die Additive Fertigung* ed R Lachmayer *et al* (Heidelberg: Springer Vieweg) pp 267–82
Welch D *et al* 2015 Construction of mouse phantoms from segmented CT scan data for radiation dosimetry studies *Phys. Med. Biol.* **60** 3589–98
Zhang H *et al* 2018 Fabrication of an anthropomorphic heterogeneous mouse phantom for multimodality medical imaging *Phys. Med. Biol.* **63** **19** 195011